

Coexistence of Multiple Conformations in Cysteamine Monolayers on Au(111)

Jingdong Zhang,[†] Ante Bilić,[‡] Jeffrey R. Reimers,[‡] Noel S. Hush,^{‡,§} and Jens Ulstrup^{*,†}

Department of Chemistry, Nano.DTU, Technical University of Denmark, DK-2800 Lyngby, Denmark, School of Chemistry, The University of Sydney, Australia, and School of Molecular and Microbial Biosciences, The University of Sydney, Australia

Received: February 15, 2005; In Final Form: May 2, 2005

The structural organization, catalytic function, and electronic properties of cysteamine monolayers on Au(111) have been addressed comprehensively by voltammetry, in situ scanning tunneling microscopy (STM) in anaerobic environment, and a priori molecular dynamics (MD) simulation and STM image simulation. Two sets of voltammetric signals are observed. One peak at $-(0.65-0.70)$ V (SCE) is caused by reductive desorption of cysteamine. The other signal, at $-(0.25-0.40)$ V consists of a peak doublet. The pH dependence of the latter suggests that the origin is catalytic dihydrogen evolution. The doublet feature is indicative of two distinct cysteamine configurations. Cysteamine monolayer formation from initial nucleation to a highly ordered phase has been successfully observed in real time using oxygen-free in situ STM. Random cellular patterns, disordered adlayer formation accompanied by high step edge mobility, and ultimately a highly ordered ($\sqrt{3} \times 4$) R30° lattice are observed sequentially. Pits are formed due to enclosure of the mobile edges during the adsorption process. In the highly ordered cysteamine layer, each unit has two spots with apparent 0.6 Å height difference in STM images. The coverage $5.7 \pm 0.1 \times 10^{-10}$ mol cm⁻² determined by voltammetry supports that the spots represent two individual cysteamine molecules. A priori MD and density functional simulations hold other clues to the image interpretation and indicate that the NH₃⁺ groups dominate the tunneling contrast. A wide range of interface structures, showing variations in the sulfur binding site and orientation, gauche and trans conformers, and especially hydrogen-bonding interactions, are examined, from which it is concluded that the adsorbate structure is controlled by interactions with the solvent rather than with the substrate.

Introduction

A major objective of interfacial engineering is control of the orientation, supramolecular organization and functional properties of immobilized molecules at the monolayer and single-molecule levels. Self-assembled monolayer (SAM) techniques offer a highly efficient tool, particularly for organic molecules with a thiol group.^{1,2} The thiol group reacts chemically with metal surfaces such as gold, forming stable metal–sulfur bonds, while a functional group at the other end controls the surface properties that can be designed for specific purposes. For example, cytochrome *c* forms functional monolayers on SAMs with a carboxylic end group on gold surfaces,^{3,4} while the blue copper protein azurin can form a monolayer on a pure alkanethiol SAM on Au(111). In either case the protein exhibits high electron-transfer rates through the carbon chain.^{5,6}

As the smallest stable ω -functionalized alkanethiol, cysteamine contains two functional groups, –SH and –NH₂, which are protonated to –NH₃⁺ in a wide pH range, one at each end of the two-carbon chain. Cysteamine has been broadly applied as a linker molecule to immobilize functional organic^{7–9} and inorganic materials^{10–12} as well as proteins^{13,14} and a metalloenzyme¹⁵ on surfaces. It has further been crucial in biofuel cell or biosensor fabrication^{16–18} and as a promoter in bioelectrochemistry.¹⁹ Interfacial SAM properties are determined by the molecular structure on the surface.²⁰ Surface techniques such

as X-ray photoelectron spectroscopy (XPS), surface enhanced Raman scattering (SERS), voltammetry, and scanning tunneling microscopy (STM) have been employed to address the structure of cysteamine monolayers on metal surfaces.^{8,21–26} Wirde et al. studied cysteamine monolayers on polycrystalline gold surfaces by XPS with focus on the S–Au bond.²¹ They also studied the oxidation of cysteamine monolayers in 50 mM phosphate buffer of pH 6.8 by cyclic voltammetry.²¹ Monolayers prepared from cysteamine hydrochloride have been examined by ex situ STM, and a $(7 \times \sqrt{3})$ superlattice structure on the Au(111) surface found.⁸ Solvent effects on the formation and quality of cysteamine monolayers have been disclosed using ex situ STM at the nanometer scale. Pit size and density in the cysteamine monolayers on Au(111) were noted to depend on the solvents.^{27–28} SERS studies were reported by Kudelski and associates, who found both gauche and trans bands on rough silver and gold surfaces.^{23–25} They observed that the cysteamine conformations strongly depend on the preparation conditions, i.e., pH, immersion time, and electrolyte. Cysteamine monolayers on gold substrates contain higher proportions of gauche bands and are more stable to the influence of electrolyte than on silver substrates.^{23–26} The conformation of molecules in solution is primarily related to interactions among solvent and solute molecules. Conformations of molecules assembling on a surface are also affected strongly by molecular intra- and interchain interactions and interactions with solvent as well as with the substrate.²⁹ Both solvent and substrate thus determine the conformation of the adsorbed molecules. In situ measurements and a priori molecular dynamics simulations of cysteamine monolayers in the presence of solvent at the molecular level

* Corresponding author. E-mail ju@kemi.dtu.dk.

[†] Technical University of Denmark.

[‡] School of Chemistry, The University of Sydney.

[§] School of Molecular and Microbial Biosciences, The University of Sydney.

are therefore highly desirable. As a surface analysis technique, in situ STM has been developed to operate directly in solution to investigate the surface structure at solid–liquid interfaces with high resolution. In situ STM enables to monitor a wide variety of electrode processes such as adsorption, dissolution, and deposition under potential control.^{30,31} Recently, in situ STM has been introduced to map functional biological macromolecules with molecular resolution in aqueous solutions.^{6,15,32,33}

In this report we address the molecular binding and conformation of cysteamine monolayers on Au(111) electrode surfaces in aqueous buffer by a combination of experimental techniques and theoretical modeling. Single-crystal voltammetry provides insight in the binding mode and functional charge-transfer properties of well-defined cysteamine monolayers on the Au(111) surfaces. This is combined with in situ STM under anaerobic conditions, described in the present work, to provide information about the supramolecular organization involving conformational details of adsorbed cysteamine at the single-molecule level. In situ STM disclosed a particularly highly ordered monolayer with $(\sqrt{3} \times 4)$ R30° surface lattice and two different cysteamine surface conformations, which match the voltammetric patterns. In addition, the cysteamine adsorption process could be followed at the nanoscale level and was found to involve lifting of the Au(111) reconstruction by nucleation of cysteamine molecules, random-cellular network formation, a disordered monolayer phase, and a highly ordered phase of the adsorbate. The voltammetric and in situ STM data have further been integrated with a priori modeling using the PW91 density functional.³⁴ The latter involves geometry optimizations and possibly also molecular dynamics (MD) simulations of the two independent ionic adsorbate molecules in a unit cell containing 15 water molecules and three layers of Au atoms. A priori computational methods were employed as the surface to headgroup interaction is extremely subtle, displaying various low-energy minima with widely differing geometrical structures and complex low-energy interconnecting paths.³⁵ Due to their intense computational demand, these calculations have not led to an extensive prediction of the interface structure, but instead have been used to examine the manifold of feasible configurations, their nature and resultant STM signature. They indicate that the most important physical properties controlling the observed structure are the solvent–adsorbate and solvent–solvent interactions.

Experimental Section

Reagents. A 5 mM NaAc (pH 6.0) sample was prepared by mixing NaAc (>99%, Suprapur, Merck) with HAc (>99.7%, Aldrich). Cysteamine (2-aminoethanethiol, >98%) was from Fluka. Cysteamine solutions were freshly prepared prior to each measurement. Milli-Q Housing (18.2 MΩ) water was used throughout.

Instrumentation and Procedures. Electrochemistry. Cyclic voltammetry was performed using an Autolab system (Eco Chemie, The Netherlands) controlled by the general-purpose electrochemical system software. Electrochemical cell and electrodes were confined in a Faraday cage in order to minimize electrical noise. The reference electrode was a freshly prepared reversible hydrogen electrode (RHE), checked against a saturated calomel electrode (SCE) after each measurement. All potentials reported are versus SCE. A clean coiled Pt wire served as counter electrode. Au(111) electrodes for both electrochemistry and STM were in-house prepared and their quality checked by the method of Clavilier and Hamelin.³⁶ The hanging meniscus method was used for electrochemical measurement. Prior to use, the Au(111) electrodes were annealed in a hydrogen flame and

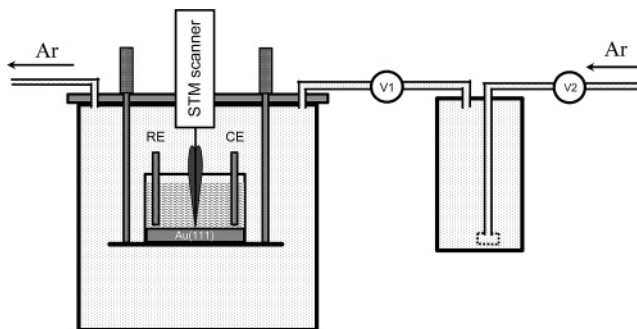


Figure 1. Schematic diagram of oxygen-free in situ STM. V1 and V2 are two valves to control smooth Ar flow. RE and CE are reference electrode and counter electrode, respectively.

quenched in Millipore water saturated with hydrogen gas. The electrodes were carefully transferred to freshly prepared cysteamine solutions. Self-assembled monolayers were formed by soaking the Au(111) electrodes in 0.5–5.0 mM cysteamine solution for 2–5 h. Electrolyte solutions were deoxygenated for several hours by Ar (5N) purified by Chrompack (oxygen < 50 ppb). All systems were blanketed with Ar-atmosphere during measurement.

Oxygen-Free in Situ STM. A Pico SPM instrument (Molecular Imaging Co., USA) was used for in situ STM. Oxygen-free in situ STM was found essential to avoid interference from oxygen in air on oxygen sensitive systems, such as cysteamine and some proteins. Figure 1 is a schematic diagram of an Ar-protected in situ STM developed in our group. The STM tip and in situ STM cell are enclosed in an Ar (5N) filled glass chamber. Mechanical turbulence and gas leakage could cause severe noise and large drift in the STM images. The glass chamber and STM scanner are therefore fixed together by airtight O-rings. Inlet and outlet allows gas flow (ca. 2.0 ± 0.5 h⁻¹) smoothly through the glass chamber during STM imaging. Two valves (V1 and V2) are used to control the gas flow. A glass bottle is employed for damping of gas turbulence before the gas enters the glass chamber. In-house built STM cells with large capacity of liquid solution (2.5–3.0 mL) are made of PTFE (Teflon). Prior to each measurement, the STM cell and tip were flushed with Ar (5N) for at least 30–40 min to remove O₂. In this way the solution in the STM cell was deoxygenated totally and a smooth stream of Ar maintained over the solution during the measurement. All STM experiments were carried out in this way. Ar protection is crucial to obtain in situ STM images of adequate quality of the cysteamine monolayer. Further investigation of this apparatus and effects on STM imaging will be discussed elsewhere. The STM scanner was calibrated against the reconstruction lines on Au(111) under the same conditions, i.e., using the same sample in the same solution (5 mM NaAc, pH 6.0) with Ar flow protection, and with the same length of tips in order to obtain accurate XY distances from the STM images. All STM images were recorded in the constant current mode. Pt/Ir (80/20, Ø 0.25 mm) tips were prepared electrochemically in a mixed solution of 1.5 ± 0.5 M CaCl₂ and 0.15 ± 0.05 M HCl at 15–25 V in AC mode at 0–4 °C. The prepared tips were insulated by Apiezon wax.

All glassware, STM cells and other utensils were cleaned prior to use as previously described.^{33,37}

Computational Methods. All calculations were performed in a three-dimensional periodic orthorhombic unit cell embodying a $(\sqrt{3} \times 4)$ R30° Au(111) surface containing three layers of Au(111) with 8 atoms per layer, 2 chemisorbed and protonated cysteamine ions SCH₂CH₂NH₃⁺, and 15 water molecules. The central layer of gold atoms was frozen in all

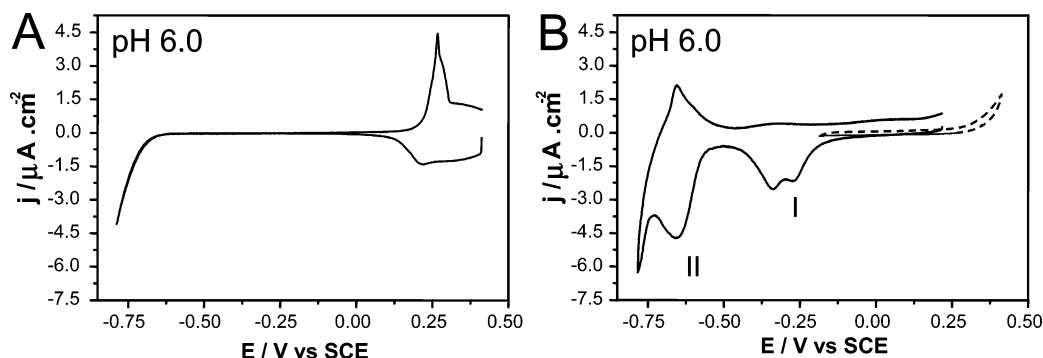
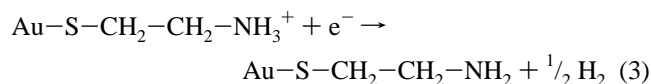
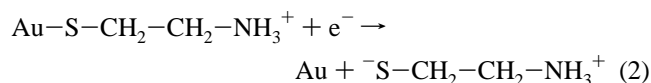


Figure 2. Cyclic voltammograms of bare Au(111) (A) and cysteamine-covered Au(111) (solid line, negative scan, dotted line positive scan) (B) in 5 mM NaAc (pH 6.0), 10 mV/s.

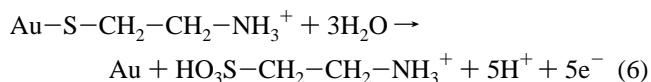
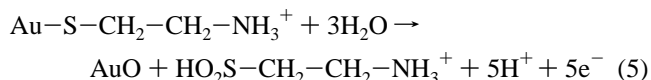
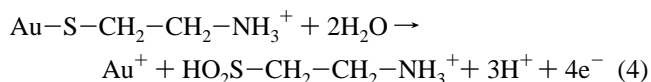
calculations, while one surface layer is bound to both cysteamines and the other surface layer confines the water molecules so as to include explicitly the structural effects caused by the presence of a nearby STM tip. While this gold slab is clearly too thin for quantitative studies, our purpose here is to determine the major qualitative features only. In effect, the total height of the unit cell, 19 Å, is partitioned into a region of ca. 5 Å containing the gold slab, with the remaining 14 Å containing the water and surface-bound cysteamine molecules. Preliminary molecular dynamics calculations at 298 K, used to estimate the liquid structure around frozen cysteamine molecules and gold lattice, were performed using the MM+ force field supplied with the HYPERCHEM program.³⁸ For the first structure considered, the unit cell height used throughout of 19.0 Å was optimized using this method to minimize the sample pressure. All preliminary structures were then optimized and possibly also processed using molecular dynamics. The VASP^{39,40} simulation package was used employing the PW91 density functional³⁵ with ultrasoft pseudopotentials^{41,42} set to an energy cutoff of 396 eV. Such molecular dynamics calculations were performed at constant volume and energy, with a time step of 1 fs and initial velocities set according to a Maxwell–Boltzmann distribution at 298 K. The Brillouin zone integration was performed on a Monkhorst-Pack $4 \times 2 \times 1$ k -point mesh with an electronic temperature of 0.2 eV. The surface unit-cell lengths were set to 5.144 Å and 11.880 Å obtained for the $(\sqrt{3} \times 4)$ R30° surface supercell of the analogously computed structure of bulk gold.⁴³

Results and Discussion

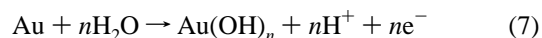
Linear and Cyclic Voltammetry. The trans conformation of cysteamine dominates in aqueous solution.²² The pK_b of cysteamine in bulk solution is about 4.5, which means that most cysteamine molecules are protonated at pH 6.0. Adsorption on metal surfaces, however, causes a significant pK_b -change. The pK_b of cysteamine monolayers on polycrystalline gold surface has been estimated as 1.8 ± 0.2 from contact-angle titration.⁴⁴ Cysteamine molecules are, therefore, protonated in the monolayer on the Au surface in pH 6.0 buffer solutions. Several reductive electrochemical processes can be envisaged:



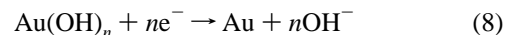
At negative potentials, reaction 1 is electrochemical dihydrogen evolution. The potential of this process depends on pH and follows the Nernst equation. Reaction 2 is reductive desorption of the Au–S bond. Reaction 3 is viewed as catalytic dihydrogen evolution through the amine group. At high potentials, oxidative desorption from the gold surface in a multiple-step process proceeds and several mechanisms with 3, 4, 5, and even 11 electrons transferred have been proposed.^{45–47} The most likely mechanisms are



Gold oxidation occurs in a similar potential range:³⁶



Gold oxide monolayers are reduced according to



To achieve quantitative analysis and avoid signal interference from the gold oxidation process, we focus on the low-potential range addressing solely adsorption and reductive desorption.

Figure 2A shows a voltammogram of bare Au(111) in 5 mM NaAc (pH 6.0) with a flat double layer region (-0.6 to $+0.1$ V vs SCE), a sharp anodic peak at 0.266 V, and a small cathodic peak at 0.218 V. The sharp anodic peak is due to the lifting of the reconstruction as well as adsorption of acetate at potentials positive of 0.26 V. Similar phenomena have been found in other inorganic buffers and discussed in detail.^{48–50} Dihydrogen evolution (equation 1) on bare Au(111) begins at -0.65 V as a tail rather than a peak. In the presence of a cysteamine monolayer, the sharp anodic peak at 0.266 V and the small cathodic peak at 0.218 V totally disappear and only a featureless double layer is seen in the voltammogram (Figure 2B dotted line, right). This means that a cysteamine monolayer has replaced the adsorption of acetate and strongly binds on the Au(111) surface. The cysteamine monolayer results in two sets of voltammetric signals, at -0.15 to -0.45 V (peak I) and -0.65 V (peak II), respectively, on the left curve in Figure 2B. A well-defined cathodic peak at -0.655 V and its corresponding anodic

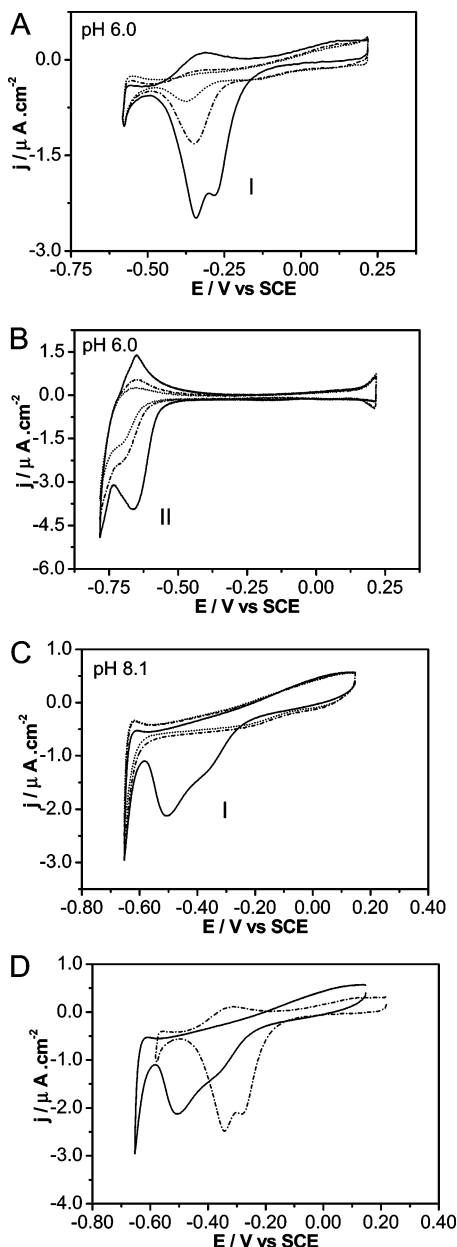


Figure 3. Cyclic voltammograms of cysteamine/Au(111) first scan (—), second scan (---), and third scan (····) in 5 mM NaAc 10 mVs⁻¹. (A) Narrow potential (+0.25 V ~ -0.60 V) and (B) full potential window (+0.25 V ~ -0.75 V) after several scans in the narrow potential window (A). Panels A and B are at pH 6.0. (C) Narrow potential window (-0.65 V ~ +0.25 V) at pH 8.1. (D) Cyclic voltammograms of cysteamine/ Au(111) first scan, pH 8.1 (solid line) and pH 6.0 (dotted line) in 5 mM NaAc 10 mVs⁻¹.

peak at -0.646 V are in contrast to the strong doublet cathodic peaks at -0.15 to -0.45 V and a broadened small anodic peak. This suggests two different origins of these Faradaic processes. This is addressed systematically below.

Voltammograms of the cysteamine monolayer on Au(111) with three consecutive scans show that peak currents from both peak I (-0.15 to -0.45 V) and peak II (-0.65 V) decrease in successive scans, indicating that other processes accompany interfacial charge transfer. Peaks I and II are therefore addressed separately in panels A and B, respectively, of Figure 3. Figure 3A shows three consecutive scans of peak I. A well-defined doublet peak at -0.278 and -0.338 V with 60 mV separation appear in the first cathodic scan direction, implying that two closely related species undertake a similar electron transfer

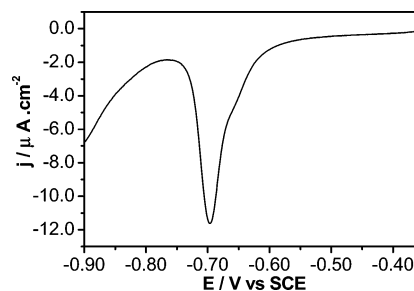


Figure 4. Linear scan voltammetry of cysteamine/Au(111) in 0.1 M NaOH, 10 mVs⁻¹.

process. The cathodic peak charges are significantly larger than those of the corresponding anodic peak. This resembles electrocatalytic behavior. However, only a single strongly decreased cathodic peak appears in the consecutive scans (Figure 3A). After peak I has totally disappeared by repeating cycling, full potential window scans are recorded in Figure 3B with only peak II. The peak potential, height, and charge from peak II are almost the same as in the original full scan in the presence of peak I. The peak current from peak II decays gradually in each scan at pH 6.1 (Figure 3B). In contrast, peak I has totally disappeared in the absence of peak II. This means that the redox process from peak II is independent of that from peak I, whereas peak I is only observed together with the peak II.

To understand the origin of the two main peaks, the pH dependence of the voltammetric behavior was addressed. The first three consecutive scans of Au(111) covered by the cysteamine monolayer at pH 8.1 are shown in Figure 3C. Peak I with doublet peaks at -0.352 and -0.519 V are seen only in the first scan. Both peak I and peak II are shifted negatively at high pH, but their voltammetric behavior is different. The shape, peak height, and charge of peak II are almost the same at pH 6.0 and 8.1, while the peak currents of the doublet in peak I are reduced to half (left) and one-third (right), and the peak separation increases from 60 mV at pH 6.0 to 167 mV at pH 8.1 (Figure 3D). In addition, the doublet of peak I is seen only in the first cathodic scan and is totally invisible in consecutive scans at pH 8.1 (Figure 3C). This is different from the behavior at pH 6.0. The voltammetric difference between peak I and peak II suggests that peak I and II have different origins. In basic solution, pH 13, peak I has totally vanished even in the first cathodic scan, whereas peak II converts into a well-defined sharp peak at the potential -0.696 V with a shoulder on the positive side (Figure 4).

It is well-known that reductive desorption of thiol-containing monolayers gives sharp voltammetric cathodic peaks in basic solution due to the cleavage of S-Au bonds. The peak potential reflects the strength of the S-Au bond while the charge of the peak corresponds to the coverage of S-Au bonds. A more negative potential indicates that more energy is needed to cleave the Au-S bond, i.e., stronger Au-S binding. The desorption peak of SAMs with short chains and hydrophilic function is shifted positively. The peak potential of the cysteamine monolayer (Figure 4) is comparable with the value for the reductive desorption of cysteine monolayers on Au(111) in the same medium, -0.705 ± 0.015 V.⁵¹ Peak II is therefore assigned to the cleavage of the Au-S bond according to eq 2. The charge of peak II in Figure 4 is measured as $5.5 \pm 0.1 \times 10^{-5}$ C cm⁻², corresponding to $5.7 \pm 0.1 \times 10^{-10}$ mol cm⁻² cysteamine on the Au(111) surface. Interestingly, as noted, there is a shoulder at -0.65 V. The shoulder is reproducible on cysteamine monolayers prepared from both Fluka and Sigma samples and appeared on all Au(111) electrodes used. This indicates strongly

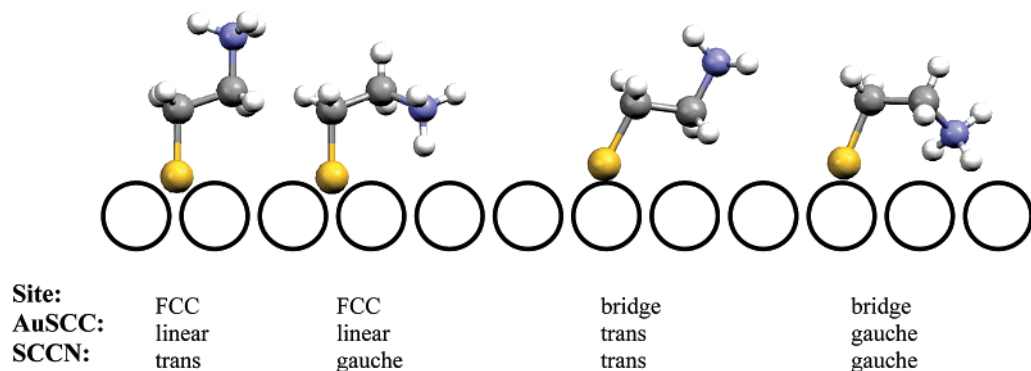


Figure 5. Some possible arrangements for cysteamine adsorbed on a Au(111) surface, showing variations in the binding site (either 3-fold FCC hollow site or 2-fold bridge site) as well as possible linear, gauche, and trans configurations for the Au–S–C–C and S–C–C–N conformations; “Au” here is taken as the point on the surface vertically beneath the S atom. Yellow, blue, and gray balls represent sulfur, nitrogen, and carbon atoms, respectively. Round circles represent gold atoms.

that the cysteamine monolayer contains two similar but distinct Au–S bond environments.

Some possible likely bonding environments are sketched in Figure 5. It has been observed⁵² that at low coverage alkanethiols assemble on gold with their SC bonds somewhat parallel to the surface while at high coverage these bonds erect vertically. A priori calculations indicate that the low inclination is associated with the sulfur atoms adopting a bridge position, bisecting two Au(111) surface atoms, while the vertical orientation is associated with sulfur binding above a FCC hollow site from where it interacts with three surface atoms.^{35,53–56}

The notion of two cysteamine conformations is supported by the properties of peak I. The origin of peak I with a doublet feature on the cathodic side can only be caused by reduction of protons through the amine group (eq 3). A doublet feature would arise, for example, if the amine group in one conformation is close to the gold surface while the amine group in the other conformation is remote from the surface. Proton binding on the amine group adjacent to the Au(111) surface needs less energy to acquire an electron from the electrode surface. This model explains several observations: (1) The first scan of peak I always gives a higher current than the second and third scan (Figure 3A). This could be due to a conformational time lag effect of proton rebinding from the solution to the amino group close to the gold surface, after electron and proton transfer from this group. This time effect is more pronounced at higher pH (Figure 3C). (2) The height of the first scan in the doublet peak I is smaller at pH 8.1 than at pH 6.0. This is most likely because the concentration of the protonated amino groups in the cysteamine monolayer at pH 8.1 is lower than at pH 6.0 since the proton concentration in the bulk solution at pH 8.1 is 2 orders of magnitudes lower than at pH 6.0. (3) Peak I is only observed together with peak II, while peak II is observed in either the absence or presence of peak I. The presence of the cathodic peak I is thus due to electron transfer after proton binding to the amino group from the electrode surface, either through the carbon chain or directly from Au(111). However, the rebinding of a proton to the amino group is thermally activated. The absence of peak I thus means that the concentration of protonated amino group in the cysteamine monolayer is too small to be detected. S–Au bond dissociation would be little affected by this process. The cathodic peak II is caused by the reduction of the S–Au bond. The absence of peak II thus means that the S–Au bonds are broken and the cysteamine monolayer has disappeared altogether from the Au(111) surface. In this case, the protonated amino groups are released together with sulfur from the electrode surface and can promote only one cathodic voltammetric signal, peak II. Steady-state rotating disk

electrode (RDE) analysis combining single-crystal electrode and RDE configurations might offer further clues to this mechanistic view but is beyond the scope of the present study.

Vibrational surface spectroscopy may hold other clues to the dual conformation of surface-confined cysteamine. We pursue here, however, a different line in which the cysteamine monolayer is addressed at the single-molecule level, namely, in situ electrochemical STM. We address this issue next.

In situ STM. Oxygen-free in situ STM was employed to investigate the formation and structure of cysteamine monolayers. Cysteamine is oxygen-sensitive and all measurements were carried out in Ar atmosphere. Figure 6 and Figure 7 show series of in situ STM images of the evolution of the reconstructed Au(111) surface during the cysteamine adsorption process. The adsorption depends on the concentration of cysteamine, adsorption time, and working electrode potential. The clean Au(111) surface is reconstructed into a herringbone pattern with $(\sqrt{3} \times 23)R30^\circ$ structure at potentials negative of -0.70 V even in the presence of cysteamine (Figure 6A). The rows of ridges on the herringbone pattern are aligned along the substrate $<1\bar{2}1>$ direction. The presence of cysteamine triggers structural evolution of the reconstructed gold surface and initiates adsorption at potentials positive of -0.70 V. The herringbone elbows present the largest areas of unfaulted 3-fold hollow sites, which are the most likely sites for critical adsorbate nucleation.⁵² Figure 6B shows that random cellular-like networks appear as a first intermediate state in the herringbone elbow sites pointed by arrow 1, while highly aligned ridge rows turn into less ordered areas. With increase of adsorption time and slight positive shifts of the working electrode potential, the nanostructured cellular networks expand and the closely packed ridges in the herringbone pattern are gradually transformed into the anisotropic shape in Figure 6C. Interestingly, small dark indented areas (indicated by arrow 2) are observed among the confined boundaries surrounded by deformed ridges. Figure 6D–E shows that the cellular network phase enlarges quickly and dominates the whole surface while the herringbone pattern is expelled almost entirely during this stage. In contrast, the dark patch domains develop steadily. Random cellular networks are encountered ubiquitously in nature despite the inherent disorder and vastly different length scales.⁵⁷ The origin of such surface structures presently is rooted in the interactions between cysteamine molecules and gold or water molecules, as well as hydrogen bonds among adsorbed cysteamine molecules. In the present study, the cellular network phase expands, but the cellular size does not increase. This is reflected in Figure 6G, which shows the surfaces fully covered by cellular networks and dark patches. The nanostructured cellular networks consti-

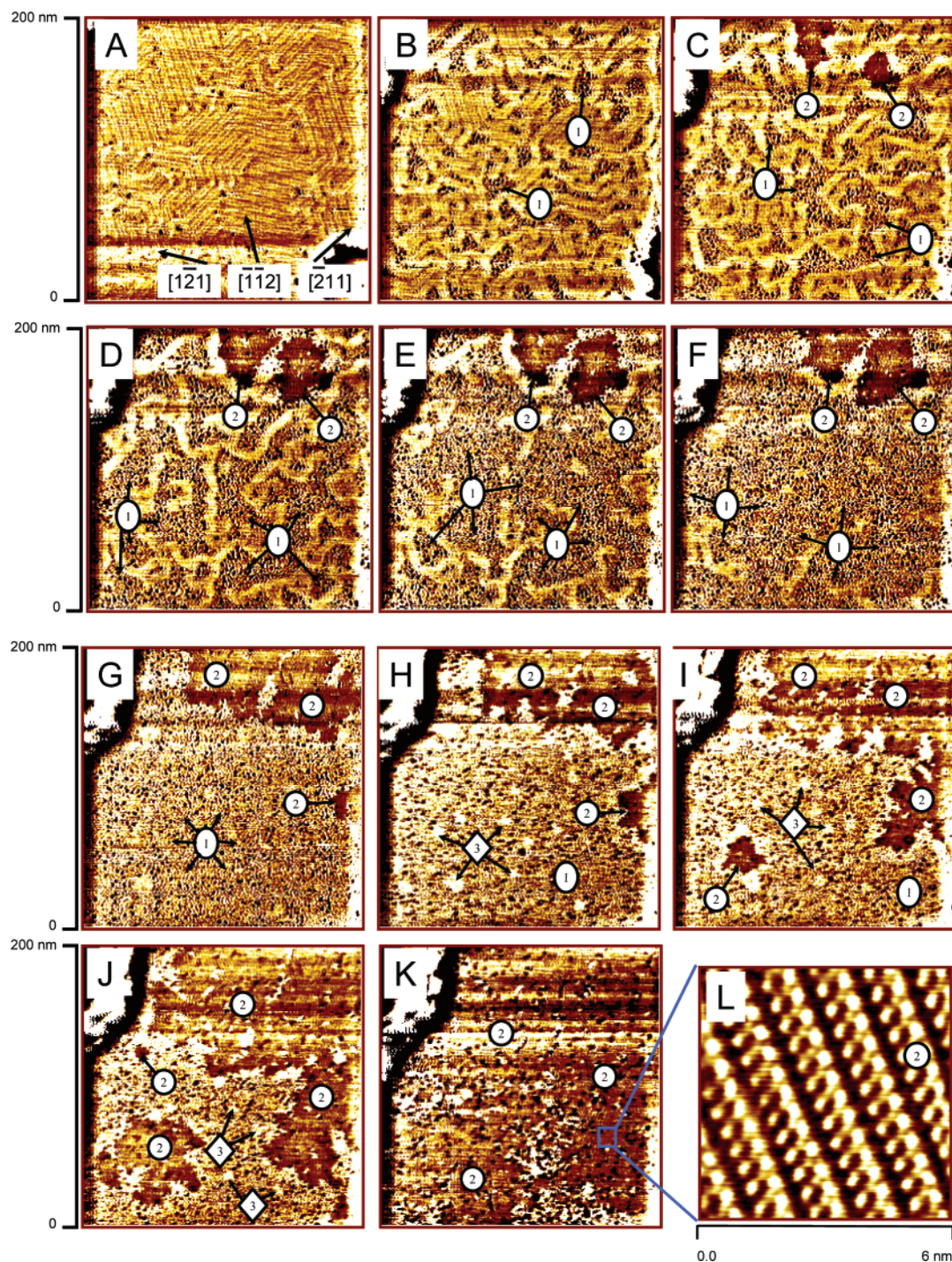


Figure 6. Oxygen-free in situ STM images of formation of cysteamine monolayer on Au(111) (domain formation). 0.8 mM cysteamine in 5 mM NaAc (pH 6.0), with Ar protection. $I_t = 0.25$ nA, $V_{\text{bias}} = -0.10$ V, except (A) -0.09 V. Working electrode potential (vs SCE) and adsorption time: (A) $E_w = -0.710$ V, 0 min 0 s; (B) $E_w = -0.680$ V, 12 min 55 s; (C) $E_w = -0.675$ V, 16 min 28 s; (D) $E_w = -0.670$ V, 20 min 36 s; (E) $E_w = -0.665$ V, 21 min 36 s; (F) $E_w = -0.665$ V, 22 min 36 s; (G) $E_w = -0.660$ V, 27 min 08 s; (H) $E_w = -0.660$ V, 28 min 09 s; (I) $E_w = -0.660$ V, 32 min 40 s; (J) $E_w = -0.660$ V, 35 min 36 s; (K) $E_w = -0.660$ V, 40 min 42 s; (L) $E_w = -0.660$ V. Scan area: (A–K) 200×200 nm² and (L) 6×6 nm².

tute an intermediate state that is replaced by a disordered adlayer, as indicated by diamond arrows 3 in Figure 6H. The disordered adlayer is further compressed and transformed into dark domains of regular structure in Figures 6I,J, though it was observed initially in Figure 6C. After annihilation of the disordered adlayer and coalescence of the dark patches, the whole Au(111) surface is finally fully covered by regular smooth dark patch domains Figure 6K, implying that the dark patch phase is in fact, the stable equilibrium state. Zooming in on the dark patch area discloses a highly ordered structure in the cysteamine

monolayer (Figure 6L). These observations suggest that the highly ordered patches constitute the matured stable state of reorganized cysteamine molecules on the gold surface.

Bare Au(111) surfaces with herringbone pattern (i.e., $(\sqrt{3} \times 23)R30^\circ$ surface lattice) are reconstructed and accommodates one extra gold atom for every 22 or 23 bulk lattice constants, giving rise to 4.3% uniaxial surface compression.^{52,58} It is reported from ultra-high-vacuum (UHV) STM that excess gold atoms are ejected from the surface layer by relaxation of the compressed herringbone reconstruction during the assembly of

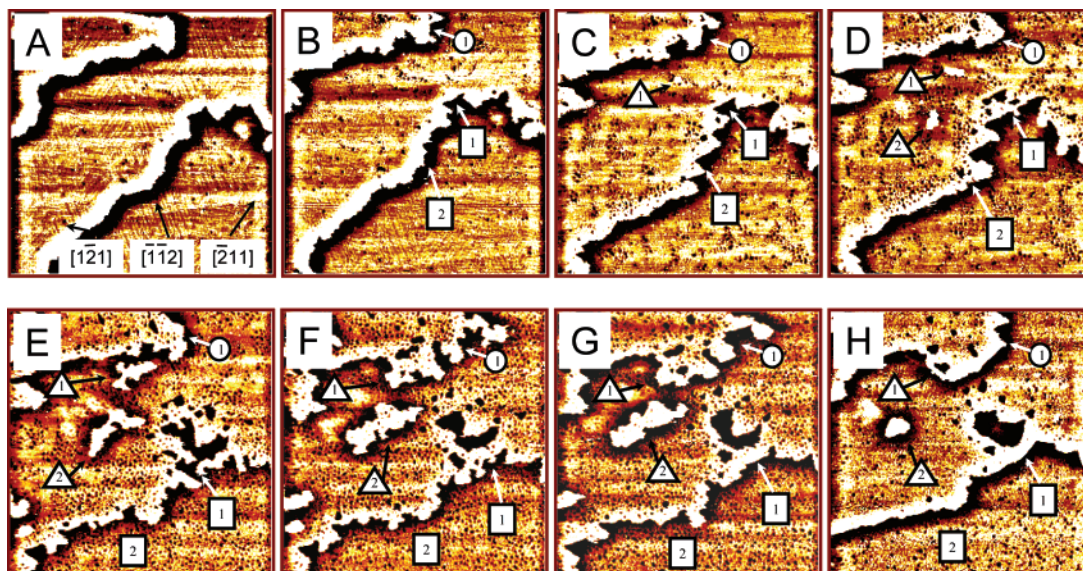


Figure 7. Oxygen-free in situ STM images of formation of cysteamine monolayer on Au(111) (pit formation). 0.9 mM cysteamine in 5 mM NaAc (pH 6.0), with Ar protection. Scan area: $200 \times 200 \text{ nm}^2$. $I_t = 0.20 \text{ nA}$, $V_{\text{bias}} = -0.06 \text{ V}$ except (A and B) $V_{\text{bias}} = -0.07 \text{ V}$. Working electrode potential: (A) $E_w = -0.68 \text{ V}$ vs SCE, (B–H) $E_w = -0.67 \text{ V}$ vs SCE. Adsorption time: (A) 0 min 0 s; (B) 2 min 0 s; (C) 3 min 0 s; (D) 3 min 30 s; (E) 4 min 0 s; (F) 4 min 32 s; (G) 5 min 32 s; and (H) 7 min 32 s.

alkanethiol monolayers on Au(111).⁵⁸ The present observation differs from both alkanethiol behavior in UHV and from cysteine and cystine adsorption dynamics on Au(111) in 50 mM $\text{NH}_4\text{-Ac}$ (pH 4.6).⁵⁹ When cystine forms monolayers on Au(111) surfaces, it was found that they induce the formation of small and highly ordered domains randomly on Au(111) terraces followed by extension into larger domains.⁵⁹ In the present study, as in situ STM shows, the cysteamine adsorption process is initiated with lift of the herringbone feature on the clean Au(111), but protrusions due to ejection of excess gold atoms do not appear. This suggests a different mechanism of formation or surface structure of cysteamine monolayers. A plausible explanation is that both the amine and thiol group in the cysteamine molecule could touch the gold surface. This may facilitate the relaxation of the gold atom contraction since the neighboring gold–gold bond lengths contract from 2.885 Å (The Au(0) surface lattice) to 2.6–2.7 Å (the radius of Au(I)⁶⁰) during formation of S–Au bonds. The carbon–carbon bond in cysteamine and hydrogen bonds among the amine groups and water molecules might be reorganized to reach metastable states toward the final stable state during the cysteamine adsorption. This accords well with the observations of nanostructured cellular networks, and a disordered adlayer followed by a highly ordered cysteamine adlayer. All these are time and potential dependent processes.

The time evolution of cysteamine-induced terrace structures offers further insight into the adsorption process. The environment of atoms inside terraces is different from that at the terrace edges, since atoms at the edge are more active due to the less coordinated adjacent atomic structures. Figure 7 shows a series of in situ STM images with focus on terrace edges on Au(111) during cysteamine adsorption. Smooth edges covered by herringbone patterns are observed before adsorption is initiated (Figure 7A). Triggered by cysteamine adsorption, terrace edges begin to “frizzle”, as indicated by circle 1 and squares 1 and 2 in Figure 7B. Edges become zigzag shaped when the random cellular structures appear and compress the herringbone structure on the Au(111) surface (Figure 7C,D). Two zigzag structures even coalesce and two small pits are enclosed inside the terrace, square 1 (Figure 7D). With increasing adsorption time, the zigzag edges covered by cellular networks further expand and

encircle each other (square 1 in Figure 7E), and a large inside “lake like” pit is formed (square 1 in Figure 7F). The edges, which fence an inside lake pit, are reorganized and result in a lake pit with larger area and a smaller perimeter (Figure 7F,G). Interestingly, two small bright pitches are deposited on the terrace near the edge, as shown by triangles 1 and 2 in Figures 7D and 7E. These two pitches extend during the maturing of the adsorption adlayer. One pitch (triangle 2) develops in two dimensions and finally shrinks into a round shape (Figures 7G,H). The other pitch (triangle 1) fuses into another edge of the terrace (close to circle 1) causing a few small pits to arise due to unification with the uneven coasts of the edge (Figures 7F,G). The height and appearance of the pitches are the same after unification with the terrace and rearrange into a smooth edge with roundish pits (Figure 7H), which are also observed for other edges of the terrace. This observation indicates that the white pitches are most likely a gold layer on which cysteamine molecules are adsorbed.

Figure 7 thus shows the microstructure evolution on terrace edges induced by cysteamine adsorption. Within 5–6 min of the adsorption process, gold atoms around the edges are found to be very mobile. Such phenomena are not seen on alkanethiol, cysteine, homocysteine, or mercaptopropionic acid monolayer formation.^{52,60–64} Amine groups in the cysteamine adlayer might thus be a determining factor in this property since the amine group is a good ligand for stable metal complexes. Pits are often found on thiolate SAMs on metal surfaces. The pit formation mechanisms have been discussed for a number of years. Etching of Au surfaces in alkanethiol solutions is reported to cause vacancy islands,⁶⁵ while ejection of gold atoms from the surface layer during relaxation of the herringbone reconstruction is suggested on the basis of evidence in UHV–STM observation for alkanethiol SAMs on Au(111).⁵⁸ Figure 7 in the present study shows that especially edges on gold surface terraces are migrant and easily encompass many pits in the initial stages of cysteamine monolayer formation. The driving force toward mobile gold surface atoms might be enhanced by the coordination of the amine group in cysteamine monolayers to surface gold atoms.

Figure 8 shows representative high-resolution STM images of stable cysteamine monolayers on a Au(111) surface. Cys-

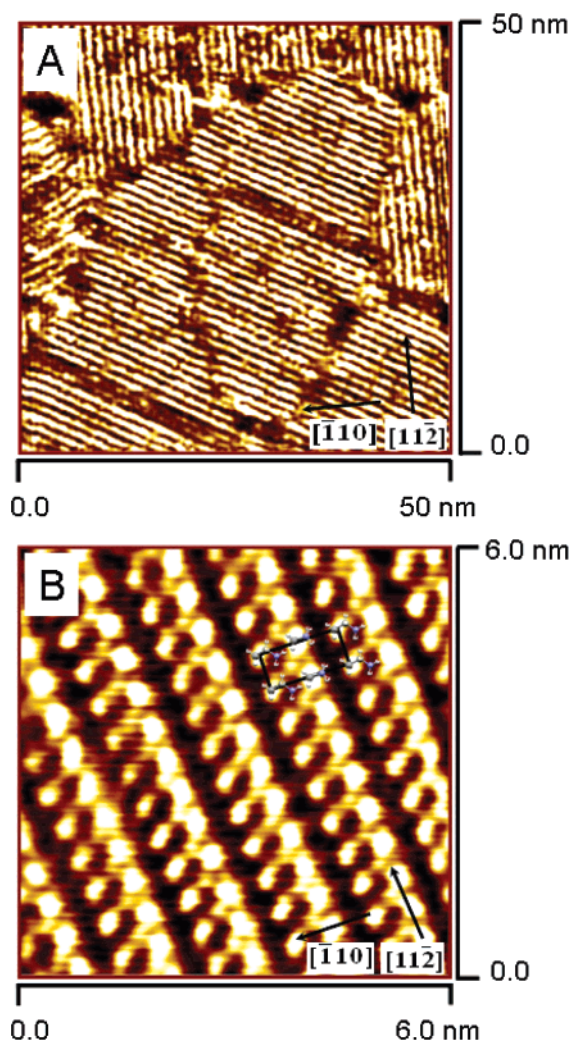


Figure 8. Oxygen-free high-resolution in situ STM images of cysteamine monolayer on Au(111) in 5 mM NaAc (pH 6.0), $E_w = -0.4$ V vs SCE, $I_t = 0.25$ nA, $V_{bias} = -0.15$ V, Ar-atmosphere. Scan area: (A) 50×50 nm² and (B) 6×6 nm². A $(\sqrt{3} \times 4)$ R30° unit cell with two cysteamine molecules are overlaid in STM image (B).

teamine forms large ordered domains in the potential range of -0.60 to $+0.20$ V vs SCE in 5 mM NaAc (pH 6.0) in an anaerobic environment. Cysteamine molecules pack into strips in domains, while small defect pits locate at the boundaries of the domains (Figure 8A). The strips are perpendicular to the atomic rows of Au(111) with a periodic distance of 11.7 ± 0.3 Å. The angle between strips in different domains is measured as $120^\circ \pm 2^\circ$, following the (111) symmetry of the substrate (Figure 8A). High-magnification STM images show that the strips are composed of rows with two different contrasts in each domain (Figure 8B). The distance between neighboring spots along rows of either contrast is 5.1 ± 0.2 Å, corresponding to $\sqrt{3}$ times of a gold atom diameter, while the distance between two nearest-neighbor weaker or stronger spots perpendicular to the strip direction is 11.7 ± 0.3 Å, close to four times the gold atomic diameter. A rectangular unit cell is therefore described as $(\sqrt{3} \times 4)$ R30° and indicated by a black box in Figure 8B. This surface structure gives a theoretical coverage of 2.88×10^{-10} mol cm⁻² according to calculated tables on the basis of geometric area.⁵¹ In fact, the S coverage measured from reductive desorption in alkali solution is $5.5 \pm 0.1 \times 10^{-5}$ C cm⁻² (Figure 4), corresponding to $5.7 \pm 0.1 \times 10^{-10}$ mol cm⁻² cysteamine on the Au(111) surface. This implies that each $(\sqrt{3} \times 4)$ R30° unit contains two cysteamine molecules. Since

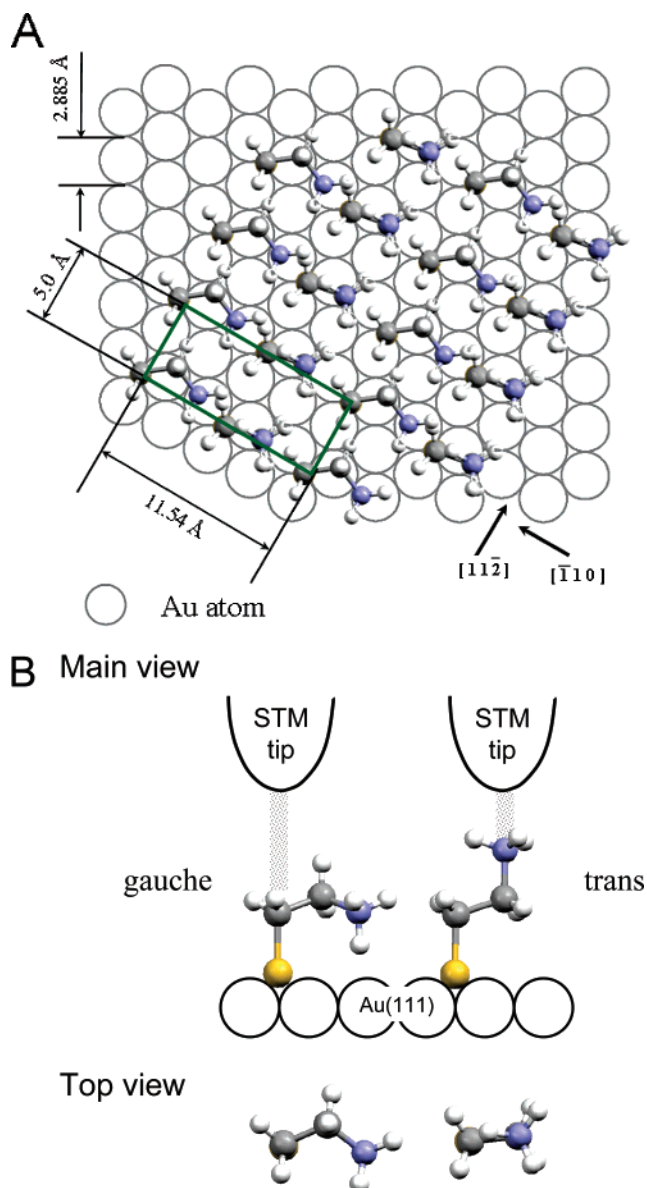


Figure 9. (A) A schematic view of one possible surface model with $(\sqrt{3} \times 4)$ R30° unit cell containing two cysteamine molecules. (B) A schematic view of tunneling paths through two possible cysteamine conformations on Au(111) surface. Main view (above) and top view (below). Yellow, blue, gray, and white balls represent S, N, C, and H atoms, respectively. Grey and black circles represent gold atoms. Cysteamine and gold are enlarged according to their real size ratio.

each $(\sqrt{3} \times 4)$ R30° unit cell in Figure 8B contains one strong and one weak spot, it is reasonable to suggest that each spot represents a different cysteamine molecule. A possible surface model with $(\sqrt{3} \times 4)$ R30° unit cell containing two cysteamine molecules was built on this basis (Figure 9A). Two possible conformations of cysteamine molecules may give different tunneling contrasts due to different tunneling paths. The model shows schematically how two possible cysteamine conformers occupy the Au(111) surface. Two cysteamine conformers are overlaid on the high-resolution STM image in Figure 8B and seen to fit geometrically the spots in the images. A theoretical approach will be discussed below.

This conclusion is evidenced by further STM observations. Some defects (dark holes in the second and third row) along the weaker-contrast rows are visualized clearly in an STM image with the same scan area and similar experimental conditions. Such defects are observed in monolayers of cysteine⁵¹ and cobalt

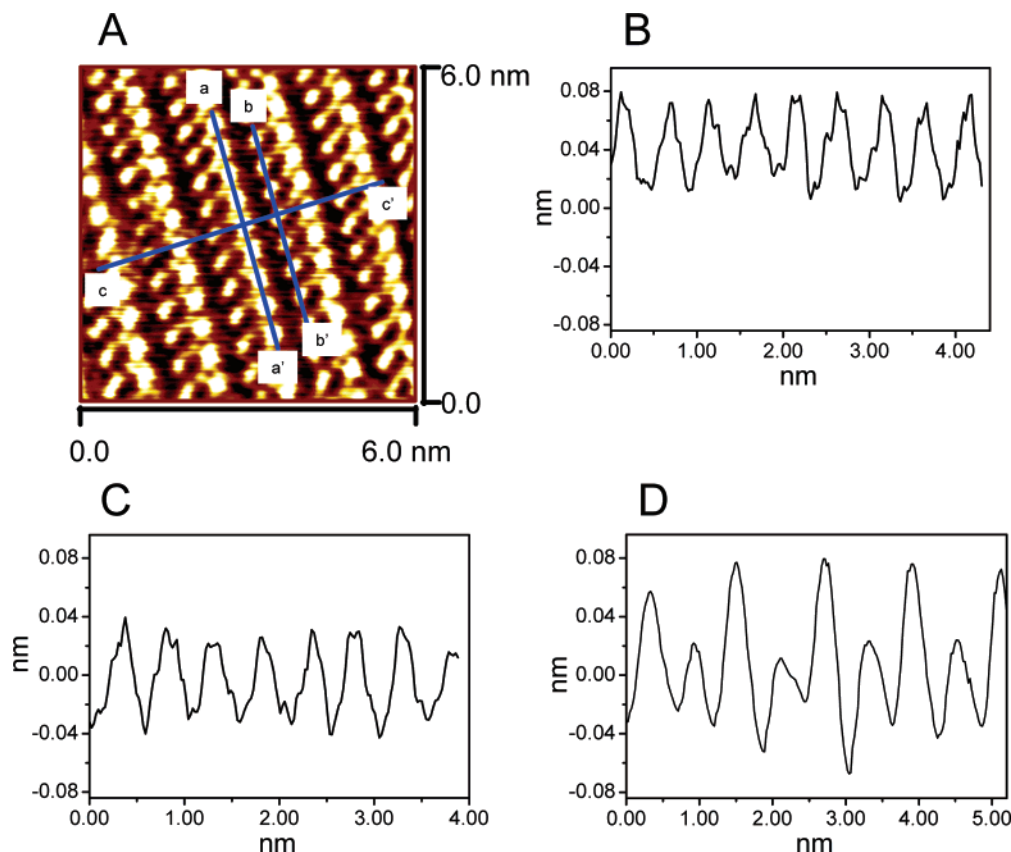


Figure 10. Cross section profiles of cysteamine STM images. (A) STM image, same condition as in Figure 8B. Panels B, C, and D are cross section profiles along the aa' , bb' , and cc' directions, respectively.

tetraphenyl porphyrin⁶⁶ on Au(111) surfaces and are regarded as a signature of missing individual adsorbate molecules. This supports the hypothesis that both the weaker and the stronger spots in the STM images are due to individual cysteamine molecules. Different contrasts for the same molecules suggest that the cysteamine molecules may adsorb on the gold surface with different conformations and provide different tunneling paths, as illustrated by a simple scheme in Figure 9 B. STM images reflect directly the tunneling current through the adsorbate molecules. The current is related to the shapes of the molecules but does not exactly represent the physical height; this aspect is explored in detail below using simulated images.

Figure 10 shows a high-resolution STM image of the cysteamine monolayer (Figure 10A) with corresponding cross section profiles along the stronger spots (Figure 10B), weaker spots (Figure 10C), and across both weak and strong spots (Figure 10D). The apparent height difference between the stronger and weaker spots is 0.6 Å while the maximum apparent height contrast observed is ca. 1.2 Å (Figure 10D). If tunneling is dominated by the same chemical functionality on each molecule (for instance, by either sulfur or the amine ions) and the sulfur binding environments are similar, then the height difference of these features above the surface is interpreted as being 0.6 Å. This could be indicative of the weaker feature arising from a molecule lying down flat on the surface, with tunneling current entering through many of its atoms, while the higher feature arises from a more upright molecule. Alternatively, the apparent tail could arise from a rapid equilibrium of different conformations for one of the cysteamines.

A Priori Simulations. The purpose of the simulations was to identify the key qualitative features responsible for the surface structure and STM image appearance. Quantitative simulations require extensive molecular dynamics simulations for the gold,

adsorbate, solvent, STM tip, and counterions under bias. While these could be made using empirical force fields, many poorly known aspects remain including the actual placement and shape of the STM tip and the role of counterions. The intricate nature of the surface to headgroup interaction, the role of weak hydrogen bonding to sulfur, and the details of the hydrophobic force involving the STM tip, define a very difficult problem for empirical force fields, however. Hence we have chosen to make *a priori* calculations using density-functional theory instead, with the consequence that extensive molecular dynamics calculations are no longer feasible and so only qualitatively indicative results are obtained.

A further complication is that the precise structure of the gold surface layer is not known; here we assume it to be an unreconstructed (111) surface. For methylthiol monolayers chemisorbed on gold, the surface is indeed to form⁶⁷ but PW91 calculations suggest that lower-energy structures with gold atom vacancies could exist.⁶⁸ In addition, methylthiol is known to chemisorb above top sites^{67,69} on the lattice while almost all calculations^{35,68} predict that such sites are significantly energetically unfavorable for the unreconstructed surface. However, as previously described, the chemisorption of cysteamine to gold shows a variety of properties different from those for methylthiol absorption and so the presence or nature of any reconstruction could vary significantly. No evidence of regular pits or protrusions in the surface is observed in the STM images, however, naively supporting the hypothesis that the surface is unreconstructed.

Results from the simulations are presented in Table 1. Initially, 24 representative structures were determined using a three-step procedure; these are listed as 1–24 in the table, where they are ordered in terms of their relative electronic potential energy ΔE . First, starting conformations for the headgroup

TABLE 1: Summary of the Structures, Energetics, and Constant-Current STM Images Obtained Using PW91 for Systems Containing Two Chemisorbed Protonated Cysteamine Ions and 15 Water Molecules Sandwiched between Au(111) Surfaces

no.	system properties ^a						cysteamine with S initially near FCC site ^b						cysteamine with S initially near bridge site ^c						STM image ^d	
	ΔE	#HB	R_{SS}	R_{SN}	R_{NN}	Δz_{NN}	AuSCC	SCCN	q	j	x	y	AuSCC	SCCN	q	j	x	y	peaks	Δz
1	0	2/2/27	5.1	4.7	4.5	-0.1	58	162	29	1	0.40	0.03	159	67	64	8	0.49	0.04	b	1.1
2	2	1/2/27	5.1	4.6	5.2	0.0	56	170	27	4	0.41	0.03	179	66	64	8	0.49	0.05	b*	1.1
2*	-14	3/2/30	4.9	5.3	6.0	1.1	128	80	61	4	0.47	0.04	151	61	60	16	0.49	0.07	f	1.24
3	3	2/3/28	5.1	5.7	5.2	-0.1	175	63	38	1	0.38	0.02	163	173	60	7	0.46	0.06	fb*	1.8
4	4	2/2/25	5.1	5.1	5.5	0.5	69	178	17	9	0.36	0.01	161	159	64	172	0.50	0.01	f	1.6
5	6	0/3/27	5.1	3.4	6.1	-2.1	48	60	22	12	0.38	0.02	164	179	60	6	0.50	0.04	b	2.6
6	7	3/3/29	5.1	6.4	4.5	-0.3	170	69	35	3	0.41	0.01	162	177	58	8	0.47	0.07	b	1.7
7	9	3/3/25	5.1	5.1	5.6	-0.1	106	171	42	8	0.41	0.02	164	172	62	175	0.51	0.02	b*	1.4
8	9	3/3/27	5.1	5.7	5.1	1.0	179	180	29	34	0.37	0.02	153	175	62	174	0.52	0.01	f	1.2
9	9	2/3/28	5.1	5.0	6.4	-0.4	1	166	17	45	0.37	0.03	160	179	60	170	0.51	0.01	b	1.0
10	9	3/2/25	5.1	4.6	6.2	-0.1	78	178	38	4	0.38	0.04	167	174	62	178	0.50	0.08	fb	0.8
10*	-8	2/2/27	4.5	4.6	5.3	0.2	65	171	16	6	0.40	0.02	113	172	68	96	0.02	0.00	f	1.1
11	11	1/6/26	5.1	3.5	4.9	-1.9	24	82	19	35	0.39	0.00	166	74	63	170	0.51	0.04	b	1.7
12	11	2/3/27	4.8	4.3	6.1	-0.3	80	175	28	6	0.38	0.00	154	165	74	46	0.93	0.01	b	1.4
13	13	2/3/26	5.1	4.8	5.8	0.4	89	174	31	6	0.39	0.04	155	170	65	2	0.48	0.10	f	1.1
14	14	2/2/28	4.7	4.1	6.2	-0.4	91	178	36	11	0.41	0.02	173	179	69	35	0.92	0.02	fb	1.1
15	17	1/2/25	5.1	3.8	6.3	-1.9	2	61	17	173	0.32	0.01	171	170	62	7	0.49	0.04		
16	18	0/3/27	5.1	3.3	6.2	-2.2	62	63	28	3	0.37	0.00	164	173	61	4	0.48	0.04		
17	22	3/2/27	5.1	5.9	5.8	0.8	171	171	37	24	0.38	0.01	179	75	59	2	0.49	0.04		
18	23	2/3/26	5.1	5.1	5.1	0.5	179	58	41	104	0.40	0.00	164	172	63	7	0.48	0.02	f*	1.5
19	24	1/2/27	5.1	3.4	6.2	-2.5	41	63	23	18	0.36	0.00	179	175	59	7	0.50	0.02		
20	24	1/1/27	5.0	3.4	6.5	0.8	69	63	29	69	0.43	0.04	83	146	55	7	0.45	0.03		
21	24	3/2/25	5.1	5.1	5.1	1.5	147	179	20	118	0.46	0.07	173	177	59	173	0.51	0.02		
22	26	2/1/24	5.1	6.0	4.1	-0.4	175	60	41	18	0.41	0.03	176	179	60	3	0.45	0.01	b	3.4
23	28	1/1/27	5.1	3.3	6.0	0.0	28	62	22	160	0.29	0.04	91	149	59	174	0.53	0.03	b	1.1
24	32	0/2/25	5.1	3.5	4.8	-2.0	53	64	26	10	0.37	0.02	172	60	63	5	0.50	0.02		
25	62	2/2/26	5.1	3.7	6.1	-2.8	87	66	33	9	0.52	0.09	128	177	37	157	0.85	0.09		
25*	27	1/2/26	3.9	3.6	4.9	-1.5	143	59	64	133	0.08	0.01	132	167	41	7	0.57	0.01	b	

^a Relative system energies, ΔE , in kcal mol⁻¹, number of hydrogen bonds #HB to NH₃⁺ of FCC-bound cysteamine/to NH₃⁺ of bridge-bound cysteamine/total #HB per unit cell; shortest intermolecular SS, SN, and NN distances, R_{SS} , R_{SN} , and R_{NN} , respectively, in Å, and vertical NN height difference Δz_{NN} . ^b For each individual cysteamine (one starting near a bridge site, the other near a FCC site), the final optimized AuSCC ("Au" here defined as the surface vertically below S) and SCCN torsional angles, in degrees, SC vector polar angles θ and ϕ in degrees, and fractional locators x and y of the S-atoms above the Au(111)-lattice, as defined in Figure 11. ^c Qualitative description of the visible features of the simulated STM images in terms of the presence of apparent image peaks associated with bridge-bound (b) and/or FCC-bound (f) cysteamine molecules, with extended ridges in the STM images indicated by *, along with the maximum calculated STM image height contrast Δz in Å.

interaction and the cysteamine torsional variables were manually entered. Second, molecular dynamics simulations were run at 298 K to optimize the structure of the water molecules within the cavity using the MM+ empirical force field. Finally, the coordinates of the entire system were optimized by energy minimization using the PW91 density functional. STM image simulations were then performed for the lower-energy structures.

As these simulations are not extensive enough to span the available configuration space, careful choice of initial conditions is essential. The surface area of the ($\sqrt{3} \times 4$) R30° unit cell is significantly larger than that required to accept two cysteamine molecules lying down, and the dark regions in Figures 8 and 9 are presumably ones in which the surface is directly exposed to the solvent. The monolayer thus appears to be analogous to alkylthiol monolayers in the low coverage regime and so bridge binding scenarios such as the two sketched in Figure 5 are expected to be important.^{35,52,53-56} Two inequivalent cysteamines per unit cell would be expected if strong hydrogen bonding occurred between the NH₃⁺ group on one molecule and the sulfur of the other. To investigate this possibility, many of the starting structures were selected with this configuration. Typically, the hydrogen-bond donor molecule was placed on a bridge site in a lying-down configuration, with the other cysteamine placed on a FCC site. The calculations thus investigated whether the low-height streaky feature in the STM images could be associated with the lying-down molecule while the higher feature could be associated with a more upright FCC-bound cysteamine.

In Table 1 the optimized structures are analyzed according to a number of intermolecular and intramolecular properties;

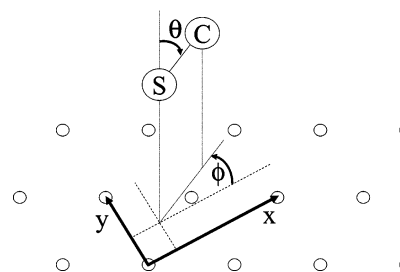


Figure 11. Fractional coordinates x and y used to describe the translation of the S atom above the Au(111) surface, and the polar angles θ and ϕ defining the orientation of the SC bond vector.

the intramolecular ones include the closest SS, SN, and NN distances, R_{SS} , R_{SN} , and R_{NN} , respectively, and the height difference between the two nitrogens, Δz_{NN} , as well as the number of hydrogen bonds on each sulfur and the total number of hydrogen bonds per unit cell. The tabulated intramolecular variables are the sulfur fractional coordinates x and y and SC-vector polar angles θ and ϕ , as defined in Figure 11, and the AuSCC and SCCN torsional angles. All the important sulfur lattice sites occur at $y = 0$ and are the FCC site ($x = 1/3$), HCP site ($x = 2/3$), bridge site ($x = 1/2$), and atop sites ($x = 0$ and $x = 1$).³⁵

Figure 12 shows some key features of the optimized coordinates for structure 2, including the location of the surface gold atoms, the structure of the cysteamine molecules, and the location of two of the water molecules, waters that fill the cavity between the cysteamine molecules and thus form a "water

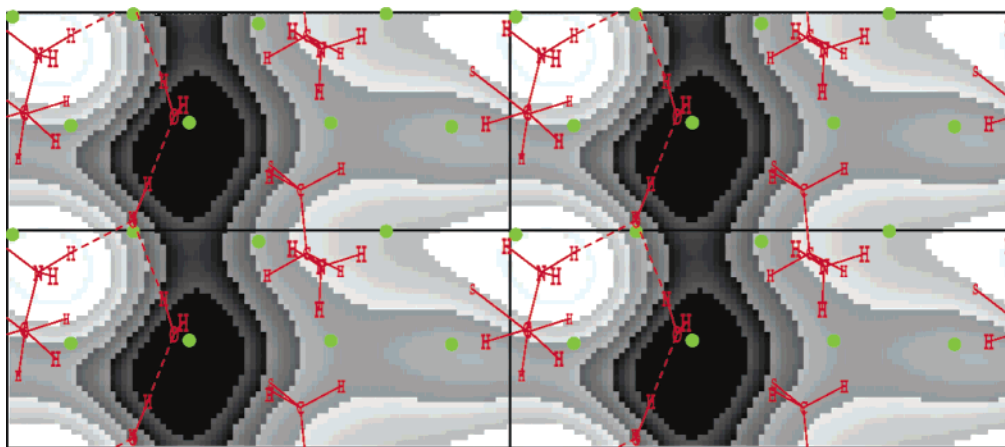


Figure 12. Simulated STM image from optimized structure 2, with the locations of the surface gold atoms shown in green as well as the cysteamine and channel-water molecules indicated in red with symbols whose size reflects the atomic height above the Au(111) surface. Four copies of the $(\sqrt{3} \times 4)R30^\circ$ surface cell are shown. The contours are the calculated electron-density isosurfaces at a density of 0.0001 au.

channel” close to the surface. Of the two cysteamine molecules, one is bonded in the bridge configuration ($x = 0.49$ from Table 1) with the more horizontal SC bond ($\theta = 64^\circ$) while the other is distorted toward the FCC structure ($x = 0.41$) with the more vertical SC bond ($\theta = 27^\circ$). Despite the strikingly different cysteamine conformations, it is noteworthy that in this structure both nitrogen atoms end up nearly equidistant from the surface.

The PW91 energy minimizations in most cases retained the initial configurations of the cysteamine molecules, as depicted in Figure 12 for structure 2. There are some notable exceptions, however, including 19 and 20, for which the S atom that was started at a bridge configuration optimized to (high local energy) atop ones. In most cases, the cysteamine that started at the (unstable) FCC structure relaxed to one of the three nearby wells in the potential-energy surface with $x \sim 0.4$; such structures have been identified as potential-energy minima for a number of thiols bound to Au(111)^{35,53–56} and are low-symmetry structures intermediate between the high-symmetry FCC and bridge ones.

To test the reliability of the force-field molecular dynamics followed by PW91 optimization approach, three structures, 2, 10, and 25, were selected for subsequent a priori molecular dynamics simulations using PW91. These simulations ran at constant energy for 1–2 ps; configurations were sampled and the geometries fully optimized, with the results for the lowest potential-energy structures so obtained are provided in Table 1 labeled 2*, 10*, and 25*, respectively. In each case, the a priori molecular dynamics resulted in significant lowering of the potential energy of the system, indicating that the original structures mainly corresponded to high-energy local minima. These simulations resulted in considerable changes to the cysteamine structures, with for 10*, one sulfur moving to a high-local-energy atop binding configuration. They, combined with the results of the previous optimizations, clearly show that the surface to headgroup interaction is subordinate to other structure determining forces. The a priori molecular dynamics simulations also induced large changes in internal cysteamine torsional angles and in the orientation of the SC bond vector, indicating that large forces had acted on the cysteamine molecules as a result of the motion of the solvent. Another manifestation of these large solvent forces is given by the total number of hydrogen bonds per unit cell, a quantity that significantly increased during the dynamics.

Little evidence was found that demonstrated the importance of NH_3^+ to S hydrogen bonds; structures containing this feature

have $R_{\text{SN}} \sim 3.3 \text{ \AA}$ in Table 1, and almost all of these are high energy ones. In an attempt to find lower energy structures of this type, the basic three-step computational procedure was modified with several configurations representing unsolvated cysteamine molecules on Au(111) were optimized using PW91 before solvation with the water molecules. The intent of this procedure was to find a strongly hydrogen-bonded environment that could possibly be maintained through to the final complete structures. Typically, the unsolvated cysteamine ions tended to dissociate from the surface, however, indicating that the Coulomb repulsion between the anions becomes the primary motive force. One structure remained bound, obtaining the expected configuration. Solvation of this structure using MM+ followed by PW91 geometry optimization resulted in the very high energy structure 25. Subsequent PW91 molecular dynamics lowered this energy considerably, producing 25*, but it is clear that cysteamine to cysteamine hydrogen-bonded structures are improbable. Again, interactions between the adsorbate and the surrounding liquid appear to dominate the monolayer structure.

The STM image simulated for structure 2 is also shown in Figure 12. This simulation is done using the Tersoff-Hamman approximation^{70,71} that relates the tunneling current to the density of states averaged from the Fermi level to the substrate applied potential. Figure 12 shows four copies of the $(\sqrt{3} \times 4)R30^\circ$ unit cell, contoured to indicate the height above the surface for a constant density of states. The brightest feature of the simulated image is associated with the NH_3^+ group of one of the cysteamines. A ridge in the simulated image runs in the direction of the long axis of the unit cell, the cc' direction from Figure 10, from this NH_3^+ group to the NH_3^+ group of the other cysteamine. Dark features in the simulated image correspond to the region above the water channel that forms between the cysteamine molecules. The simulated image is quite similar to the observed one, the only qualitative difference being that the observed tunneling goes through a minimum in the intervening region. Continuing in this long-axis direction, both the observed and simulated images become dark, and the two images are in excellent agreement in this region; it is identified as one in which the solvent molecules directly approach the gold substrate. Quantitatively, the experimental images show a height contrast of ca. 1.2 Å, while the calculated one, is given in Table 1 as $\Delta z = 1.1 \text{ \AA}$.

Of all the simulated STM images, the one shown in Figure 12 most closely resembles those observed. In most other cases, however, no resemblance was found at all. Generally, the highest

features on the simulated images are associated with the NH_3^+ groups. Both these moieties and the sulfur lone pairs have orbitals in the region of the metal Fermi energy and so both are expected to facilitate tunneling; the close proximity of the lowest-unoccupied molecular orbital of NH_3^+ to the Fermi energy is guaranteed as charge transfer from the metal destabilizes this orbital until it becomes so aligned. In all structures, the NH_3^+ groups are much higher above the surface than are the S atoms and hence they dominate the simulated tunneling. No tunneling occurs to the tip directly from the carbon atoms of the wide-band-gap intermediary alkane chain, however, suggesting that it is unlikely that the cause of the observed streaks in the STM images is tracking of the alkane chain.

The simulated STM images are described in Table 1 qualitatively in terms of whether one or both of the cysteamines give rise to a local maximum in the predicted tunneling current, and whether a tunneling ridge is predicted akin to that in Figure 12. Quantitatively, the maximum height contrast Δz is also given, as is the vertical separation between the two nitrogens, Δz_{NN} . Two factors are seen to affect whether two local maxima appear in the tunneling current: the height difference and the sulfur binding site. The effect of the binding site does not appear to be able to offset for more than a 0.4 Å difference in the actual height of the NH_3^+ groups, however. For example, structure 2, used to produce the image shown in Figure 12, has no significant height difference, but the brightest cysteamine is bound to a bridge site with a gauche SCCN configuration while the other cysteamine is bound to the mixed FCC-bridge site with a trans SCCN configuration. The observed STM images have considerably sharper features than the simulated ones. Hence it is feasible that the ca. 0.6 Å observed apparent feature height difference is due to two cysteamines with the same binding topology but with different chain conformations placing the NH_3^+ groups at heights above the surface differing by 0.6 Å.

The microscopic information provided by the simulations provides insight into the electrochemical splitting of 0.06 eV shown in Figure 3A between the two components of peak I. If this difference is attributed entirely to the stabilization of a charge through interaction with a metal surface, then the potential difference would be $3.6 \text{ V/Å} \times (1/z_1 - 1/z_2)$, where z_1 and z_2 are the heights above the surface of the two nitrogen atoms. The simulations produce optimized heights in the range 2.8–6.6 Å, but all low-energy structures with symmetrical hydrogen bonding have heights in the range of 4–6 Å only. If the observed STM feature height difference of 0.6 Å from Figure 10 does in fact reflect an actual nitrogen height difference, then from these equations the predicted splitting in peak I would be 0.07–0.12 V, in qualitative agreement with the observed value. This analysis is based on the assumption of similar solvation of both cysteamine ions. From Table 1, the hydrogen bonding analysis indicates that large energy fluctuations are associated with increasing or decreasing the number of hydrogen bonds formed to the NH_3^+ groups. Such fluctuations would give rise to much larger splittings in peak I than is actually observed, suggesting that the two hydrogen bonding environments are in fact quite similar. This result is consistent with the earlier observations made from the results of the simulations that the solvation forces are the most significant ones.

Conclusions

Cyclic voltammetry has shown that cysteamine forms stable monolayers on Au(111) in its protonated form over a range of applied potentials. The monolayers are reductively deprotonated to their neutral form at the potential $-(0.25\text{--}0.40) \text{ V}$ versus

SCE, while the monolayers are lost due to reductive desorption of Au–S bonds as the potential is dropped further to $-(0.65\text{--}0.70) \text{ V}$ versus SCE. Oxygen-free in situ STM is used to follow the complex path by which the protonated cysteamine monolayers form, transforming the surface from its clean reconstructed herringbone pattern through a random cellular phase at low coverage to a disordered phase, and finally to a highly ordered $(\sqrt{3} \times 4) \text{ R}30^\circ$ monolayer containing two distinct cysteamine molecules per unit cell.

The monolayer coverage is $5.7 \pm 0.1 \times 10^{-10} \text{ mol cm}^{-2}$. This is sufficiently low to preclude two cysteamine molecules in their fully extended conformation lying flat on the surface from covering all the available surface area per unit cell. A priori computations using the PW91 density functional indicate that a wide range of conformations and binding site variations are possible with extended lying-down conformations being unfavorable. Hence, the complete monolayer leaves significant fractions of the gold surface exposed to the solvent. The calculations indicate that solvation of the cysteamine NH_3^+ ions dominates the monolayer structure; the solvation forces appear to be much larger than those associated with the surface to headgroup interactions, intercysteamine hydrogen bonding, and internal cysteamine conformational variations.

Simulation of the STM images indicates that the dominant tunneling processes at low bias involve the NH_3^+ groups. The observed STM images contain two distinct local maxima, with each maximum associated with one of the two cysteamines per unit cell. Their apparent height difference is 0.6 Å; the simulated images indicate that up to 0.4 Å in apparent height could possibly be associated with tunneling modulation induced by different surface to headgroup binding topologies, with the remaining height difference being attributable to actual height differences of the NH_3^+ groups above the surface. The observed 0.06 eV splitting in the cyclic voltammetric peaks associated with deprotonation of the NH_3^+ groups is consistent with strong and equivalent hydrogen bonding to both groups, being controlled instead by the varying image-charge stabilization due to the nearby metallic surface.

The equilibrium structure of the solvent between the monolayer and the STM tip will depend significantly on the shape and height of the tip above the surface as well as on the properties of the associated counterions. As the monolayer structure is sensitive to the solvent structure but because of its relatively low surface density and is independent of cysteamine packing forces, the high-resolution aspects of the STM images may not be intrinsic ones but rather ones that result from the scanning procedure. Such a phenomenon is unusual in STM applications and may indeed be due to the ionic nature of the adsorbate. Nevertheless, it is clear that the primary qualitative feature revealed by the STM images, the presence of two distinct cysteamine molecules on the surface, is a property of the unperturbed monolayer as is clearly demonstrated in the cyclic voltammograms.

Acknowledgment. Financial support from The Danish Technical Science Research Council and from the Australian Research Council is acknowledged. We greatly appreciate the assistance from the workshop at Department of Chemistry, Technical University of Denmark, as well as the computational resources provided by the Australian Partnership on Advanced Computing.

Supporting Information Available: Oxygen-free in situ STM images showing the formation of a cysteamine monolayer on Au(111) (domain formation) with 65 successive STM images

and the formation of a cysteamine monolayer addressing the terrace edges of Au(111) with 16 successive STM images. This material is available free of charge via the Internet at <http://pubs.acs.org>.

References and Notes

- Schreiber, F. *Prog. Surf. Sci.* **2000**, 65, 151.
- Poirier, G. E. *Chem. Rev.* **1997**, 97, 1117.
- Song, S.; Clark, R. A.; Bowden, E. F.; Tarlov, M. J. *J. Phys. Chem.* **1993**, 97, 6564.
- Avila, A.; Gregory, B. W.; Niki, K.; Cotton, T. M. *J. Phys. Chem. B* **2000**, 104, 2759.
- Chi, Q.; Zhang, J.; Andersen, J. E. T.; Ulstrup, J. *J. Phys. Chem. B* **2001**, 105, 4669.
- Zhang, J.; Chi, Q.; Kuznetsov, A. M.; Hansen, A. G.; Wackerbarth, H.; Christensen, H. E. M.; Andersen, J. E. T.; Ulstrup, J. *J. Phys. Chem. B* **2002**, 106, 1131.
- Katz, E. Y.; Solov'ev, A. J. *Electroanal. Chem.* **1990**, 291, 171.
- Kawasaki, M.; Sato, T.; Yoshimoto, T. *Langmuir* **2000**, 16, 5409.
- Kawasaki, M.; Sato, T. *J. Phys. Chem. B* **2001**, 105, 796.
- Mirkhalaf, F.; Schiffrin, D. J. *J. Chem. Soc., Faraday Trans.* **1998**, 94, 1321.
- Cheng, Z.; Cheng, L.; Gao, Q.; Dong, S.; Yang, X. *J. Mater. Chem.* **2002**, 12, 1724.
- Arias, F.; Godinez, L. A.; Wilson, S. R.; Kaifer, A. E.; Echegoyen, L. *J. Am. Chem. Soc.* **1996**, 118, 6086.
- Willner, I.; Shabtai, V. H.; Katz, E.; Rau, H. K.; Haehnel, W. *J. Am. Chem. Soc.* **1999**, 121, 6455.
- Katz, E.; Shabtai, V. H.; Willner, I.; Rau, H. K.; Haehnel, W. *Angew. Chem. Int. Ed. Engl.* **1998**, 37, 3253.
- Zhang, J.; Welinder, A. C.; Hansen, A. G.; Christensen, H. E. M.; Ulstrup, J. *J. Phys. Chem. B* **2003**, 107, 12480.
- Katz, E.; Filanovsky, B.; Willner, I. *New J. Chem.* **1999**, 481.
- Willner, I.; Katz, E.; Patolsky, F.; Buckmann, A. F. *J. Chem. Soc. Perkin Trans. 2* **1998**, 1817.
- Kharitonov, A. B.; Zayats, M.; Alfonsa, L.; Katz, E.; Willner, I. *Sensors Actuators B* **2001**, B76, 203.
- Karlsson, J. J.; Nielsen, M. F.; Thuesen, M. H.; Ulstrup, J. *J. Phys. Chem. B* **1997**, 101, 2430.
- Lahann, J.; Mitragotri, S.; Tran, T. N.; Kaido, H.; Sundaram, J.; Choi, I. S.; Hoffer, S.; Somorjai, G. A.; Langer, R. *Science* **2003**, 299, 371.
- Wirde, M.; Gelius, U.; Nyholm, L. *Langmuir* **1999**, 15, 6370.
- Kudelski, A.; Hill, W. *Langmuir* **1999**, 15, 3162.
- Michota, A.; Kudelski, A.; Bukowska, J. *Langmuir* **2000**, 16, 10236.
- Michota, A.; Kudelski, A.; Bukowska, J. *J. Raman Spectrosc.* **2001**, 32, 345.
- Michota, A.; Kudelski, A.; Bukowska, J. *Surface Science* **2002**, 502–503, 214.
- A.; Kudelski, J. *J. Raman Spectrosc.* **2003**, 34, 853.
- Lee, S. Y.; Noh, J.; Ito, E.; Lee, H.; Hara, M. *Jpn. J. Appl. Phys.* **2003**, 42, 236.
- Lee, S. Y.; Noh, J.; Hara, M.; Lee, H. *Mol. Cryst. Liq. Cryst.* **2002**, 377, 177.
- Yokoyama, T.; Yokoyama, S.; Kamikado, T.; Okuno, Y.; Mashiko, S. *Nature* **2001**, 413, 619.
- Gewirth, A. A.; Niece, B. K. *Chem. Rev.* **1997**, 97, 1129.
- Itaya, K. *Progr. Surf. Sci.* **1998**, 58, 121.
- Hansen, A. G.; Boisen, A.; Nielsen, J. U.; Wackerbarth, H.; Chorkendorff, I.; Andersen, J. E. T.; Zhang, J.; Ulstrup, J. *Langmuir* **2003**, 19, 3419.
- Chi, Q.; Zhang, J.; Nielsen, J. U.; Friis, E. P.; Chorkendorff, I.; Canters, G. W.; Andersen, J. E. T.; Ulstrup, J. *J. Am. Chem. Soc.* **2000**, 122, 4047.
- Perdew, J. P.; Wang, Y. *Phys. Rev. B* **1992**, 45, 13244.
- Bilic, A.; Reimers, J. R.; Hush, N. S. *J. Chem. Phys.* **2005**, 122, 094708–1.
- Hamelin, A. *J. Electroanal. Chem.* **1996**, 401, 1.
- Chi, Q.; Zhang, J.; Friis, E. P.; Andersen, J. E. T.; Ulstrup, J. *Electrochem. Commun.* **1999**, 1, 91.
- HYPERCHEM 5.1 Pro; Hypercube Inc., 1997.
- Kresse, G.; Hafner, J. *Phys. Rev. B* **1993**, 47, RC558.
- Kresse, G.; Furthmüller, J. *Comput. Mater. Sci.* **1996**, 6, 15.
- Vanderbilt, D. *Phys. Rev. B* **1990**, 41, 7892.
- Kresse, G.; Hafner, J. *J. Phys. Condens. Matter* **1994**, 6, 8245.
- Bilic, A.; Reimers, J. R.; Hush, N. S.; Hafner, J. *J. Chem. Phys.* **2002**, 116, 8981.
- Yu, H. Z.; Zhao, J. W.; Wang, Y. Q.; Cai, S. M.; Liu, Z. F. *J. Electroanal. Chem.* **1997**, 438, 221.
- Fawcett, W. R.; Fedurco, M.; Kovacova, Z.; Borkowska, Z. *J. Electroanal. Chem.* **1994**, 368, 265.
- Loglio, F.; Schweizer, M.; Kolb, D. M. *Langmuir* **2003**, 19, 830.
- Yang, D. F.; Maznai, H. A.; Morin, M. *J. Phys. Chem. B* **1997**, 101, 1158.
- Magnussen, O. M. *Chem. Rev.* **2002**, 102, 679.
- Bunge, E.; Nichols, R. J.; Roelfs, B.; Meyer, H.; Baumgartel, H. *Langmuir* **1996**, 12, 3060.
- Zhang, J.; Chi, Q.; Andersen, J. E. T.; Hansen, A. G.; Nielsen, J. U.; Ulstrup, J. *Probe Microscopy* **2001**, 2, 151.
- Zhang, J.; Chi, Q.; Nielsen, J. U.; Friis, E. P.; Andersen, J. E. T.; Ulstrup, J. *Langmuir* **2000**, 16, 7229.
- Poirier, G. E.; Pylant, E. D. *Science* **1996**, 272, 1145.
- Gottschalk, J.; Hammer, B. *J. Chem. Phys.* **2002**, 116, 784.
- Hayashi, T.; Morikawa, Y.; Nozoye, H. *J. Chem. Phys.* **2001**, 114, 7615.
- Yourdshahyan, Y.; Rappe, A. M. *J. Chem. Phys.* **2002**, 117, 825.
- Duwez, A.-S. *J. Elect. Spectrosc. Relat. Phenom.* **2004**, 134, 97.
- Moriarty, P.; Taylor, M. D. R.; Brust, M. *Phys. Rev. Lett.* **2002**, 89, 248303–1.
- Poirier, G. E. *Langmuir* **1997**, 13, 2019.
- Zhang, J.; Chi, Q.; Nielsen, J. U.; Hansen, A. G.; Andersen, J. E. T.; Wackerbarth, H.; Ulstrup, J. *Russ. J. Electrochem.* **2002**, 38, 68.
- Conway, B. E. *Ionic Hydration in Chemistry and Biophysics*; Elsevier: Amsterdam, 1981.
- Poirier, G. E. *Langmuir* **1999**, 15, 1167.
- Poirier, G. E.; Fitts, W. P.; White, J. M. *Langmuir* **2001**, 17, 1176.
- Zhang, J.; Demetriou, A.; Welinder, A. C.; Albrecht, T.; Nichols, R. J.; Ulstrup, J. *Chem. Phys.*, in press.
- Zhang, J.; Christensen, H. E. M.; Ooi, B. L.; Ulstrup, J. *Langmuir* **2004**, 20, 10200.
- Edinger, K.; Golzhauser, A.; Demota, K.; Woll, C.; Grunze, M. *Langmuir* **1993**, 9, 4.
- Yoshimoto, S.; Tada, A.; Suto, K.; Narita, R.; Itaya, K. *Langmuir* **2003**, 19, 672.
- Kondoh, H.; Iwasaki, M.; Shimada, T.; Amemiya, K.; Yokohama, T.; Ohta, T.; Shimomura, M.; Kono, K. *Phys. Rev. Lett.* **2003**, 90, 066102–1.
- Molina, M. L.; Hammer, B. *Chem. Phys. Lett.* **2002**, 360, 264.
- Roper, M. G.; Skegg, M. P.; Fisher, C. J.; Lee, J. J.; Dhanak, V. R.; Woodruff, D. P.; Jones, R. G. *Chem. Phys. Lett.* **2004**, 389, 87.
- Tersoff, J.; Hamann, D. R. *Phys. Rev. Lett.* **1983**, 50, 1998.
- Tersoff, J.; Hamann, D. R. *Phys. Rev. B* **1985**, 31, 805.